Diurnal variation of precipitation over the Indo-China Peninsula:

Two-dimensional numerical simulation

By Takehiko Satomura

Division of Earth and Planetary Science, Graduate School of Science, Kyoto University, Kyoto, Japan

Abstract

The diurnal variation of precipitation over the Indo-China Peninsula is investigated using a two-dimensional, nonhydrostatic, and cloud-resolving numerical model. The model is initialized by the climatological monthly mean vertical profiles of zonal flow, temperature and humidity at the center of the Indo-China Peninsula in June.

The model successfully simulates the diurnal variation of precipitation. The simulated diurnal variation is as follows: convection is activated at the lee-side foot of two mountainous regions located at the west and middle of Thailand in the evening of each day; activated clouds then are organized into squall lines that travel eastward during the night at about 5–10 m s^{-1}. These squall lines weaken around midnight.

It is concluded that the solar-synchronized life cycle of the squall lines and their eastward movement cause the nighttime maximum of the precipitation over the inland area of the Indo-China Peninsula. High resolution analysis of a convective activity index calculated from the GMS IR data over the Peninsula supports this conclusion.

1. Introduction

Convective cloud systems in the tropics release huge amounts of latent heat and play an important role in driving the global circulation of the atmosphere. The temporal and spatial distributions of the cloud systems determine the time and place of the heat release. In the tropics, the diurnal variation is a prominent time scale.

Diurnal variability of precipitation over land in the tropics and mid-latitude summer have been studied observationally using rain gage networks (e.g., Wallace 1975; Schwartz and Bosart 1979; Landin and Bosart 1985; Riley et al. 1987; Oki and Mushiake 1994) and radars (e.g., Karr and Wooten 1976; Saito and Kimura 1998). Although a rain gage network observes precipitation directly, it occasionally misses local precipitation. A long time series of rain gauge measurements reduces this deficit. Using hourly rain gauge data extending over 7–35 years, Wallace (1975) and Riley et al. (1987) studied diurnal variations of precipitation in both warm and cold seasons in the United States. Both papers

Corresponding author: T. Satomura, Division of Earth and Planetary Science, Graduate School of Science, Kyoto University, Kitashirakawa Oiwakecho, Sakyo-ku, Kyoto 606-8502, Japan. E-mail: satomura@kugi.kyoto-u.ac.jp.

found that, in the warm season, the phase of diurnal precipitation cycle has a prominent maximum in the evening (around 1800 local time) in the lee of the Rockies. Their analysis also revealed that, as one moves eastward, a clear transition to a nocturnal maximum occured over the high plains during the warm season. Wallace (1975) suggested that mountain-generated precipitation systems tended to move eastward over the Central Plain after sunset, but didn't identify the type and mechanism of the system. Using radar data in Japan, the fact that the phase of daily precipitation cycle in summer has a nocturnal maximum was also observed in the northwestern part of the Kanto Plain near the mountains (Saito and Kimura 1998). Likewise, they did not discuss the attendant mechanisms in detail.

Oki and Mushiake (1994) analyzed the seasonal and diurnal cycle of tropical precipitation (Malaysia) in addition to precipitation in Japan using hourly rain gage data extending more than 10 years. A pronounced peak of rainfall at 1600 local time in inland regions of the Malay Peninsula and a morning peak on the windward coast for the monsoon wind were found. The eastward or westward shift of the maximum phase of diurnal precipitation was not analyzed in the inland regions. It should be noticed that the width of Malay Peninsula is about 300 km, which is much shorter than the distance

from the Front Range of the Rockies to the central United States.

Infrared outgoing radiation or infrared equivalent black body temperature (T_{BB}) is used to study large-scale cloud activity. An index of T_{BB} , which selects T_{BB} lower than a threshold value and averages over several degrees in longitude and latitude, corresponds well with precipitation (e.g., Reed and Jaffe 1981; Richard and Arkin 1981; Arkin and Meisner 1987); it is used to study diurnal variability of precipitation over a wide area (e.g., Reed and Jaffe 1981; Albright et al. 1985; Duvel and Kandel 1985; Meisner and Arkin 1987; Janowiak et al. 1994; Nitta and Sekine 1994; Harada et al. 1998). By these studies, the continent/ocean contrast is now well known; the diurnal cycle of precipitation has a 1800 to 0000 local time maximum over the tropical continents and a morning maximum over the ITCZ. Using three-hourly infrared data from a geostationary satellite, Meisner and Arkin (1987) reported an eastward phase shift of the diurnal cycle near the eastern boundary of the Rocky Mountains similar to the shift analyzed by rain gages (Wallace 1975). Asai et al. (1998) analysed diurnal variability of cloudiness over East Asia during the warm season and also showed that a systematic phase delay similar to the east of the Rocky Mountains appeared to the east of the Tibetan Plateau. It is also possible through the analysis of Nitta and Sekine (1994) to distinguish the analogous eastward phase shift of the diurnal cycle of precipitation in July over the Indo-China Peninsula, although this phase shift was not discussed in their paper.

Nowadays, a numerical model is a powerful tool. The accuracy of amount, location and time of precipitation in global numerical models is of great importance in simulating the climate of the Earth. Randall et al. (1991) examined diurnal variability of precipitation in a general circulation model (GCM) and concluded that the model simulated the afternoon maximum over the land in warm rainy seasons and an early morning maximum over the oceans far from land. Apart from the causes which they presumed (see recent arguments of Sui et al. 1998, or Liu and Moncrieff 1998), the early morning maximum over the ocean apparently agreed with observation. The afternoon maximum over the land discorded with the analyses using rain gages (e.g., Wallace 1975) and T_{BB} (e.g., Meisner and Arkin 1987; Nitta and Sekine 1994), however; the reason of this discrepancy is not understood.

A few papers on the diurnal variation of precipitation over the Indo-China Peninsula have been published. Although the analyzed area of Murakami (1983) included the Indo-China Peninsula, he focused on the diurnal variability over the ocean and the Tibetan Plateau. Nitta and Sekine (1994) also analyzed the wide area included the Indo-China

Peninsula, but focused on the diurnal variability over the ocean. Both papers used infrared irradiance data with a resolution of 1° longitude-latitude square mesh of comparable resolution to GCMs. Their analyses are, therefore, unable to detect systems too small to be simulated properly in GCMs that may contribute the night maximum of diurnal variation of precipitation over the tropical continent. Infrared irradiance data of 0.1° resolution were analyzed over the Indo-China Peninsula by Harada et al. (1998). They discussed the land/ocean contrast, spatial variation over the Peninsula, and an intraseasonal variation of the diurnal cycle of T_{BB}. They also noticed a movement of cloud systems from north to south. The mechanism which produces night maximum of diurnal precipitation cycle was, however, not fully discussed.

The purpose of this paper is to study the diurnal variation of precipitation over the Indo-China Peninsula during the monsoon period using a numerical model. To describe cloud behavior accurately, a nonhydrostatic cloud-resolving model is employed with cloud microphysics and interactive radiation. Since the statistical behavior of the diurnal cycle of precipitation is the focus herein, the initial condition of the model is taken from climatic data.

2. Numerical model and experimental setup

The numerical model used in this study is based on RAMS (Regional Atmospheric Modeling System) developed by Colorado State University and the *ASTER division of Mission Research Corporation. The detailed description of RAMS was given by Pielke et al. (1992). It was configured as a two-dimensional, nonhydrostatic and compressible equation model in our study. Surface-layer fluxes were parameterized using a vegetation model (Avissar and Pielke 1989). Vegetation type was specified as the "evergreen broad leaf forest"; that is, one of 18 possible types based on the BATS (Biosphere-Atmosphere Transfer Scheme; Dickinson et al. 1986). A bulk microphysical parameterization including the ice phase was used to simulate clouds. A radiation code adopting the DOM/adding algorithm and a semi-random overlapping model (Nakajima et al. 1995) was used in place of the RAMS radiation parameterizations.

The horizontal grid spacing is 935 m, while the vertical spacing is stretched from 25 m at the lowest level to a maximum of 500 m. The vertical grid is a terrain-following coordinate system (Gal-Chen and Somerville 1975; Clark 1977). The coordinates in this system (x^*, z^*) are defined as:

$$\begin{cases} x^* = x \\ z^* = H\dfrac{z - z_s}{H - z_s}, \end{cases} \qquad (1)$$

where H is the height of the model top and z_s is the

bottom topography height. The horizontal and the vertical domains used 1600 and 65 grid points, and reached approximately 1500 km horizontally and 26 km above the sea level, respectively.

The upper boundary is a rigid horizontal surface. Above a height of 16 km, an absorbing layer is utilized to avoid the reflection of vertically-propagating waves at the upper boundary. At the lateral boundaries, a radiative boundary condition (Klemp and Wilhelmson 1978) is applied to the velocity component normal to the boundary. All variables other than the normal velocity component have zero gradient at lateral inflow boundaries and are set values at outflow boundaries such that the second spatial derivative is zero.

Topography is a highly filtered form of the actual topography transecting 95°E 14°N and 105°E 17°N through the middle of Indo-China Peninsula (Fig. 1a). This is approximately parallel to the tropospheric mean wind direction over the Indo-China Peninsula in June (see below). Figure 1b compares the smoothed topography that was used in the model to the actual topography with 30″ longitude resolution. About 290 km from the left (west) and about 200 km from the right (east) boundaries, the lower boundary of the model domain is the sea; the Andaman Sea and the South-China Sea, respectively. Mountains around $x \approx 400$ km are the Dawna Range, which separate Myanmar from Thailand, and $x \approx 1200$ km are the Annam Range which separate Laos from Vietnam. The region between $x \approx 800$ and 1100 km is the Khorat Plateau, north-eastern Thailand. The peaks around $x \approx 700$–800 km correspond to the Dong Phraya mountains. Because the model domain is oriented approximately west-to-east, the right-hand direction and the left-hand direction in the model domain are hereafter referred to as eastward and westward, respectively.

The initial thermodynamic and wind conditions were specified by an interpolation from climatic values on June at 102.5°E 17.5°N, about the center of the model domain. A profile over an upstream (western) point was not employed for the initial condition because upstream profiles over the ocean are not representative of the Indo-China Peninsula which is the focus herein. Figure 2 shows the climatic vertical profile of thermodynamic variables and wind. The wind velocity along the model domain is depicted as U and the wind perpendicular to the model domain is depicted as V. Because V is much smaller than U except in the lowest 1 km, only U is considered. The sea surface temperature is kept constant at 302 K according to the climatic sea surface temperature of the Andaman Sea in June. The climatic vertical profiles in June is practically the same as the profiles in July. The difference of U is less than 1 m s^{-1} for the lower troposphere
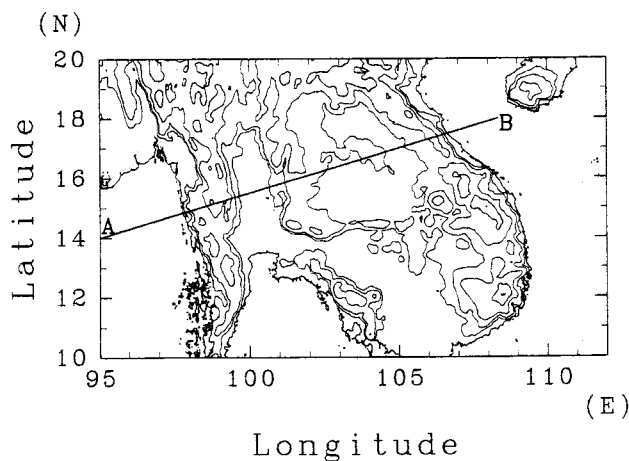

Fig. 1a. Topography of the Indo-China Peninsula. Surface elevation is contoured at 100 m, 200 m, 500 m and 1000 m. Thick line A–B is the section used in our 2-D model.
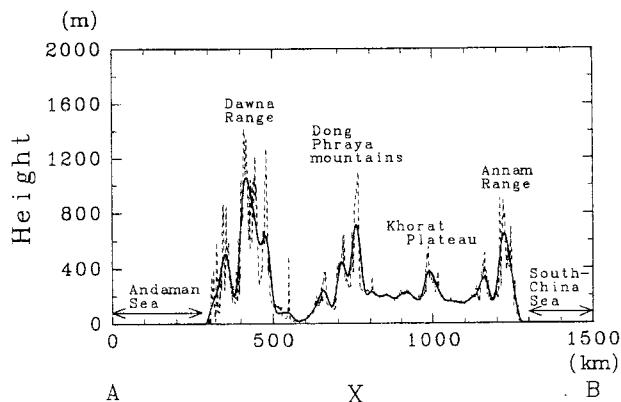

Fig. 1b. Model input topography (solid line) and unfiltered topography with 30″ longitude resolution (dashed line).

(> 400 hPa) and linearly increases to 4.5 m s^{-1} at 100 hPa where U is about 25 m s^{-1}; the temperature difference is less than about 0.5 K throughout most of the troposphere; and the difference of the mixing ratio is less than 3×10^{-4} kg kg^{-1}. Therefore, the climatic vertical profiles in June are a representative vertical profile of the early-to-mature monsoon season in the Indo-China Peninsula.

The experimental conditions described is hereafter referred to as CNTL. In addition, the following three experiments were performed (Table 1):

1) remove mountains and make all the land flat (referred to as NOMNT);

2) remove seas and set all the model lower boundary to be land with the same surface elevation as CNTL (referred to as NOSEA);
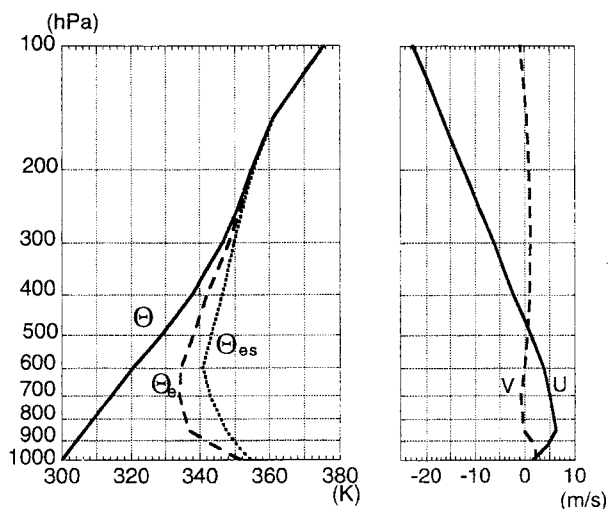
Fig. 2. Vertical profiles of Initial conditions. Left: potential temperature (solid), equivalent potential temperature (dashed) and saturated equivalent potential temperature (dotted). Right: wind velocities parallel (solid) and perpendicular (dashed) to the model domain.

Table 1. Experimental conditions.

Run	Mountain	Sea	Moisture
CNTL	yes	yes	yes
NOMNT	no	yes	yes
NOSEA	yes	no	yes
DRY	yes	yes	no

3) same as CNTL except microphysical processes are removed (referred to as DRY).

These experiments are obviously intended to clarify the effects of mountains, the sea surface and the condensation by comparing with CNTL.

All simulations began at 00 LST of Thailand (17 UTC) and were integrated for 3 days. An initial random disturbance was added to the temperature at the lowest atmospheric layer with an amplitude of 1 K.

Experiments using topography made from two other sections through the Indo-China Peninsula were completed; along the 16°N line and the transecting line 95°E 15°N and 105°E 18°N. Experiments using initial thermodynamic and wind conditions on June at 95°E 15°N over the Bay of Bengal also performed. However, results of these simulations is not shown because they are essentially the same as the results of CNTL.

3. Results

3.1 CNTL simulation

3.1.1 Diurnal variation

On the first day of the integration, convection scattered over the land area during daytime. On the second and third days, rather organized convective systems developed over the land in the afternoon and some remained active until midnight. The evolution of condensate is displayed in Fig. 3 for 6-hour intervals on the third day. At midnight, weak convective systems remained over the eastern half of the land area (Fig. 3a) and disappeared in the morning (Fig. 3b). In the daytime (Fig. 3c), convective activity was still weak over the land except over the upstream (western) slope of the Dawna Range. In the evening, a strong convective system formed over the downstream (eastern) foot of the Dawna Range (Fig. 3d). As on the second day, this system moved eastward during the night.

A horizontal-time section diagram of precipitation rate averaged on the second and the third days is shown in Fig. 4. As noticed in Fig. 3, precipitation was rarely observed in the early morning except near the eastern boundary. The lower boundary for $x > 1300$ km is sea and the early morning or pre-dawn maxima of precipitation over this region is similar to the observed diurnal cycle of precipitation over the ocean (e.g., Sui et al. 1997). Precipitation in this region is, however, not discussed further because the lateral boundary will affect its characteristics. In late morning, precipitation was simulated over the upstream side of the Dawna Range ($x \approx 400$ km). This precipitation system moved from the west to the mountains, but did not pass over the Range (1000-m high). Therefore, the precipitation continued over the upstream slope of the Range until evening. In the downstream side of the Dawna Range, a precipitation system began developing in the afternoon at $x \approx 450$–500 km. This system moved eastward with a speed of about 7 m s^{-1} until midnight and reached the western slope of the Dong Phraya mountains around $x \approx 700$ km. Another significant precipitation system developed also over the eastern (downstream) side of the Dong Phraya in the evening and moved eastward till midnight at about 10 m s^{-1}. Over the western slope of the Dong Phraya, precipitation occurred in the afternoon but was weak.

On inland areas that are far eastward from mountainous regions, the simulated diurnal variation of precipitation showed a peak at night or at midnight. Precipitation systems which started at the eastern foot of the mountainous region in the late afternoon each day, and moved eastward with a speed of 7 10 m s^{-1}, caused nighttime maxima of precipitation on those inland areas.
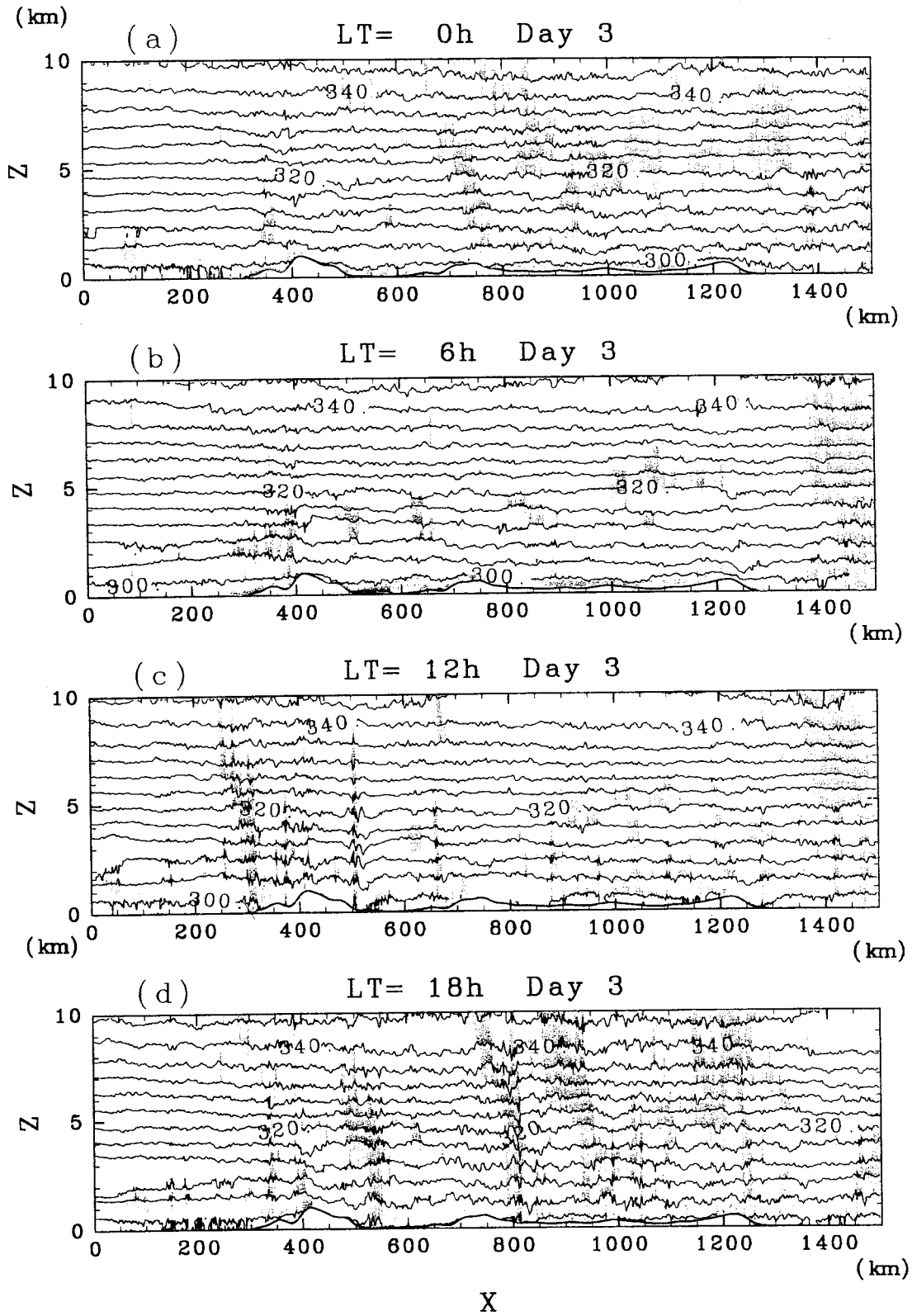
It should be noticed that a clear spacial gap of

Fig. 3. Predicted potential temperature and condensates at (a) $t = 0$ h, (b) $t = 6$ h, (c) $t = 12$ h and (d) $t = 18$ h on the third day in case CNTL. The mixing ratio of condensates in excess of 10^{-4} kg kg^{-1} (cloud boundary) is shaded. Contour interval for potential temperature is 4 K. Time coordinate is local standard time in Thailand (= UTC + 7 h).
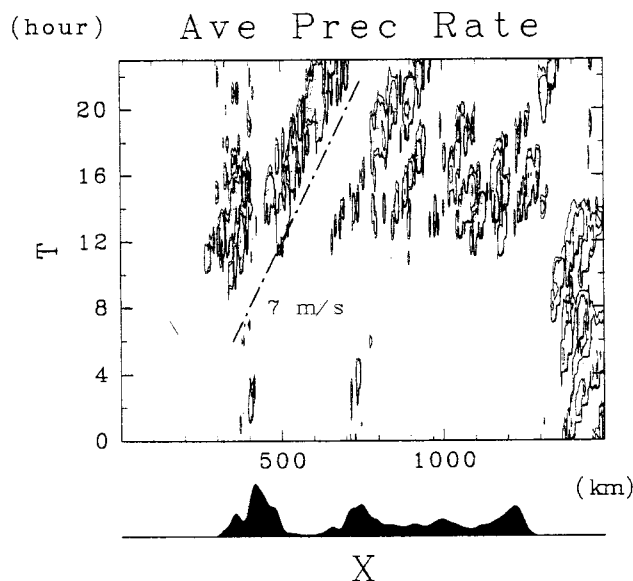
Fig. 4. Horizontal-time section diagram of precipitation rate averaged on the second and the third days in case CNTL. Contours of precipitation are 0.5, 1 and 10 mm h^{-1}. Shaded area indicates precipitation rate is greater than 1 mm h^{-1}. Dash-dotted line indicates moving speed of 7 m s^{-1}. The surface topography is depicted by the black shading at the bottom of the figure.
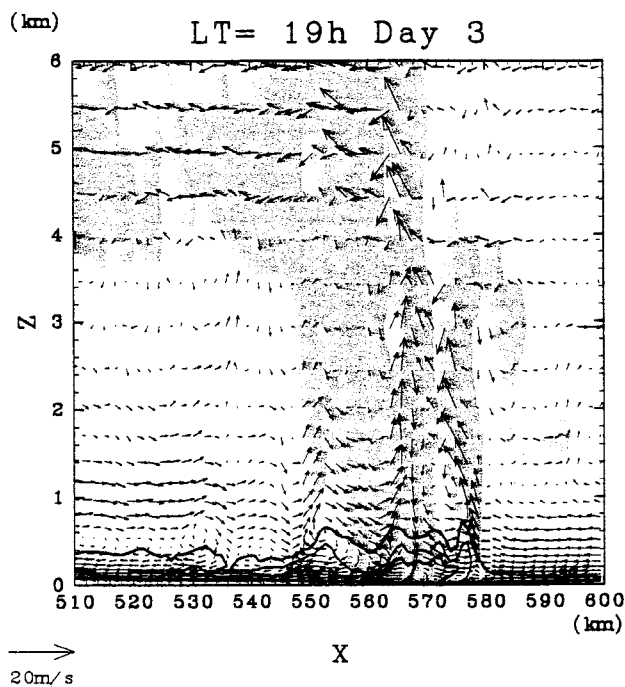

Fig. 5. Close-up of a precipitating area at $t = 19$ h on the third day in case CNTL. Shading depicts regions of mixing ratio of condensates greater than 10^{-4} kg kg^{-1}. Solid lines are potential temperature $\theta \leq 300$ K with 1 K interval. Winds relative to a system moving with 7 m s^{-1} are represented by arrows. A 20 m s^{-1} reference vector is shown on the lower left. Vertical wind velocities are exaggerated by a factor of 5.

precipitation existed at just downstream of the peak of the Dawna Range ($x \approx 400$–450 km). Another precipitation gap was also found just downstream of the peak of the Dong Phraya ($x \approx 750$ km) although it was narrow.

3.1.2 Structures of the moving precipitation systems

A close-up of a precipitation area moving to the right (eastward) in Fig. 5 displays two precipitation shafts at $x \approx 560$ km and $x \approx 570$ km. Ahead of the precipitation shafts, a new cloud was triggered by the cold pool beneath it. The cold pool was 2–3 K colder than the environment and its depth was about 500 m. Significant front-to-rear flow was noticed in the lowest 1 km in front of the cold pool and in the trailing clouds of 4–6 km height, which extended for $x < 550$ km. Strong upward motion in convective clouds occurred at the front of the precipitation system and connected the lower and upper front-to-rear flow. A region of strong upward motion and condensate showed down-shear tilting. Under the trailing clouds rear-to-front flow was found from 0.6 to 2 km in height. A part of the rear-to-front flow ascended at $x \approx 550$ km and 565 km, and the other part descended into the cold pool. These structures are similar to tropical squall lines (e.g., Moncrieff and Miller 1976; Zipser 1977; Chong et al. 1987; Hauser et al. 1988; Tao and Simpson 1989).

Figure 6 portrays a time sequence of vertical ve-

locity and condensate for 70 min period between 18 h 10 min and 19 h 20 min on the third day. In Fig. 6a, four cells of vertical velocity can be seen. Near the front of the precipitation system, a new cell formed above the leading edge of the cold pool located at $x = 550$ km. Further rearward were decaying cells above $x = 545$ and 535 km, and an older cell at $x = 527$ km above an accompanying rain shaft.

Subsequent panels, each separated by 10 min, show that the new echo first intensified and then decayed as it moved rearward relative to the cold pool. By 19 h 0 min (Fig. 6f), another new cell formed at the leading edge of the cold pool. The location of the new cell relative to the cold pool was the same as for the new cell of Fig. 6a; this behavior of the simulated multi-cell system allows us to define the model system's propagation speed as that of the cold pool. An updraft always existed above the cold pool front, which supports the advective cell regeneration in multicell storm proposed by Lin et al. (1998).

A density current propagation speed equation derived by Seitter (1986) is
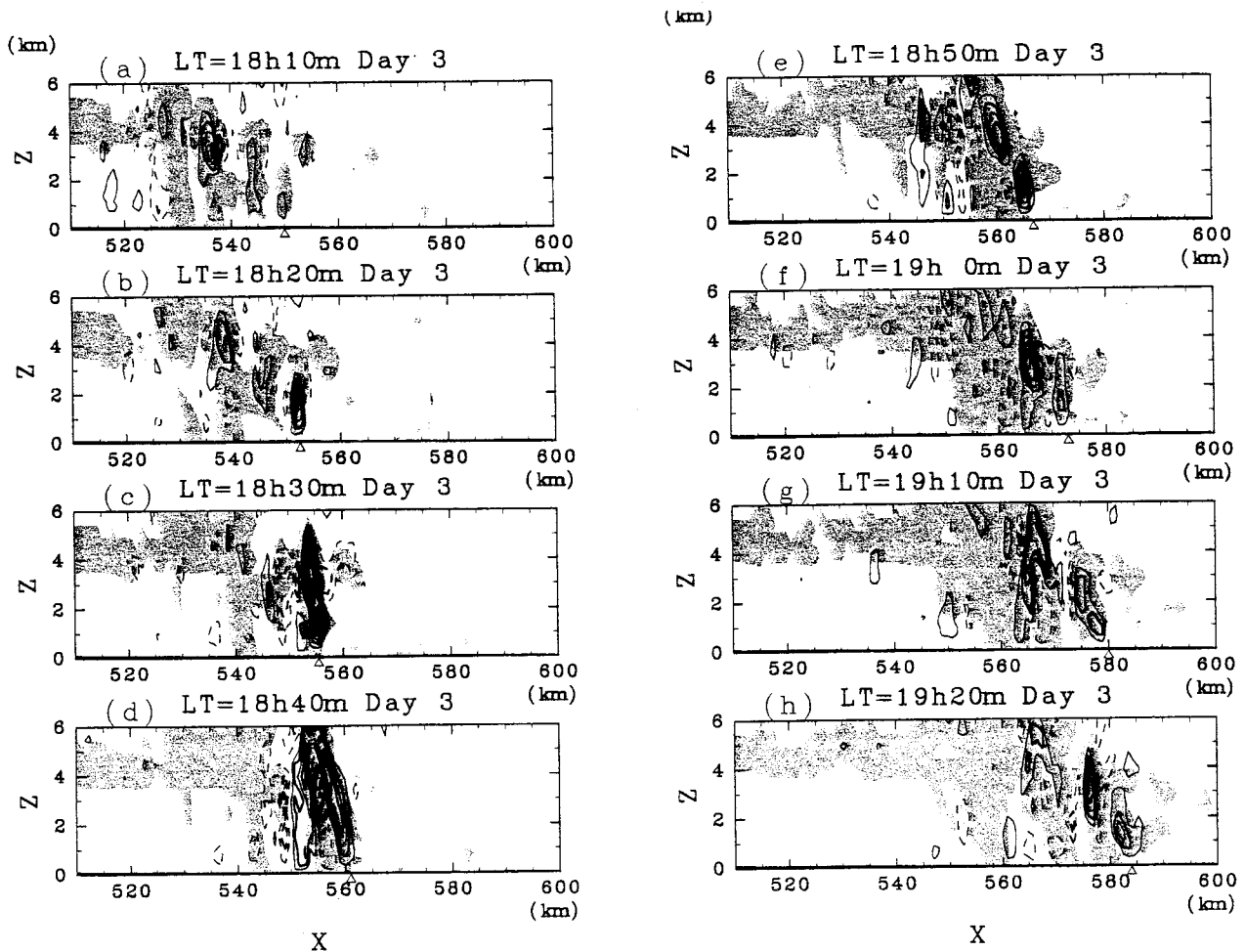
Fig. 6. Vertical velocity and condensates presented for 10 min intervals between 18 h 10 min and 19 h 20 min in the third day in case CNTL. The same 90 km section of the domain as in Fig. 5 is displayed. Vertical velocity is contoured with 1 m s^{-1} interval. Solid and dashed contours indicate positive and negative velocities, respectively. Shaded region encloses mixing ratio of condensates greater than 10^{-4} kg kg^{-1}. Open rectangle at the x axis indicates the position of the front edge of cold pool.

$$V = k\sqrt{\frac{\Delta p}{\rho}}, \qquad (2)$$

where V is the velocity of the front, Δp is the difference in surface pressure between the density current head and the environment, ρ is the density of the environment. The constant k is approximately unity. In case of the system shown in Fig. 5, $\Delta p \approx 50$ Pa and $\rho \approx 1.16$ kg m^{-3}. An ambient wind in the evening in this region is almost calm. The density current speed V estimated from parameters in this precipitation system is ~ 6.5 m s^{-1}, which is close to the travel velocity of the system (~ 7 m s^{-1}). This result indicates that simulated precipitation systems were not simply advected by the low level wind but rather propagated at the speed of the gravity current.

Since structures were similar to the squall lines and moving speeds were close to the gravity currents, precipitation systems simulated in this study will simply be called squall lines hereafter.

3.1.3 Origin of the squall lines

The squall lines were initiated over the leeward foot of the mountains in the afternoon and propagated eastward. This initiation and propagation repeated every day, resulting in the night maxima of precipitation in the inland region. Hence, the triggering location and time of squall lines govern the diurnal cycle of precipitation over the Indo-China Peninsula.

Figure 7 shows a close-up time sequence of wind velocity, condensates and potential temperature for the 45 min period between 16 h 00 min and 16 h 45 min on the third day around the Dawna Range. At 16 h (Fig. 7a), a deep layer of cold air began to travel on the downstream side of the mountain, but not beyond the lee slope far from the mountain peak in the daytime. The cold air over the windward side of the mountain was maintained by the relatively cold sea surface temperature of the Andaman Sea and also by precipitation systems over the windward side of the Dawna Range that screened the solar ra-
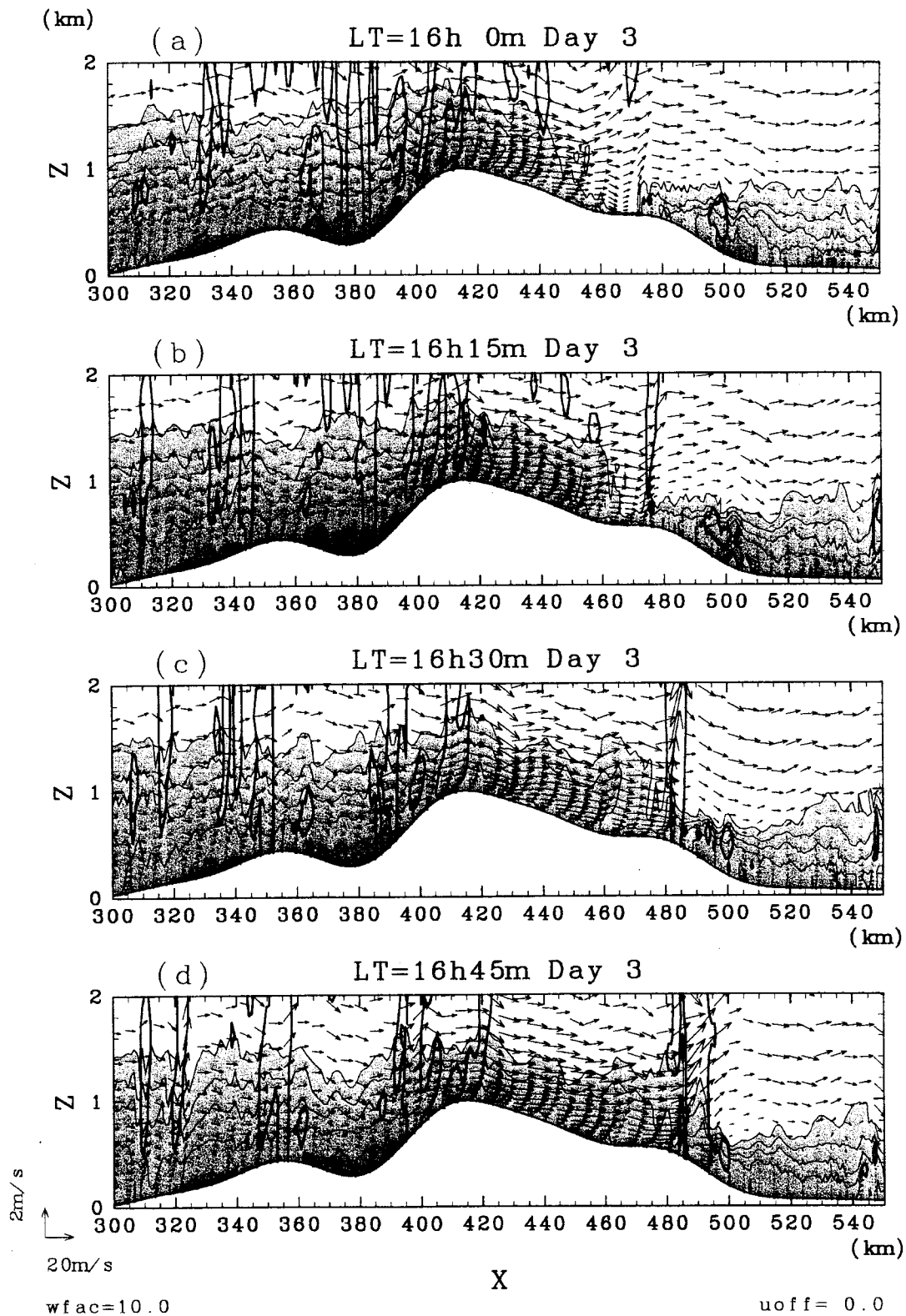
Fig. 7. Close-up around the Dawna Range presented for 15 min intervals between 16 h and 16 h 45 min on the third day in case CNTL. Shading depicts regions of potential temperature $\theta \leq 302$ K with contour line of 1 K interval. The boundary of mixing ratio of condensates in excess of 10^{-4} kg kg^{-1} (cloud boundary) is drawn by a heavy thick line. Winds are represented by arrows. A 20 m s^{-1} and 2 m s^{-1} reference vectors are shown on the lower left.
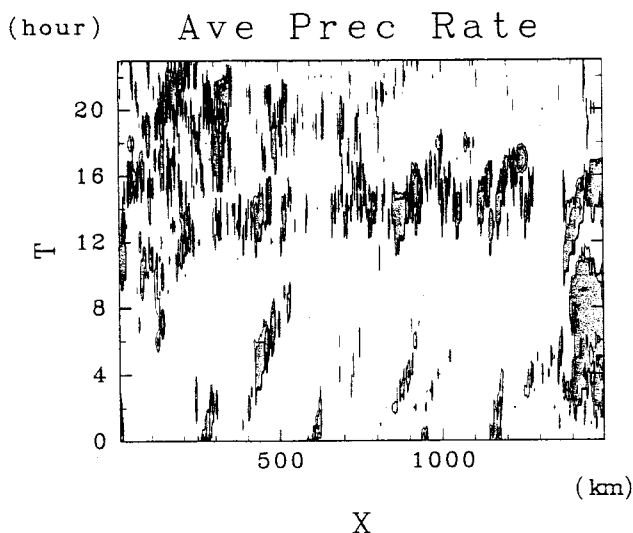
Fig. 8. Same as Fig. 4 except for case NOMNT.

Fig. 9. Same as Fig. 4 except for case NOSEA.

diation and cooled the air through evaporation of precipitation. Subsequent panels in this figure, each separated by 15 min, show that the cold air penetrated further on the lee side (Fig. 7b) and finally triggered deep convection at $x = 485$ km (Fig. 7c). This started to propagate eastward (Fig. 7d).

Although precipitation continued over the windward side of the Dawna Range during the daytime, clouds advected from the windward side to the lee side dissipated and considerable precipitation did not occur on the lee slope between 420 km $< x <$ 470 km. Downslope wind on the lee slope prevented the air parcel from lifting and reaching condensation level; this resulted in the precipitation gap remarked on in Fig. 4.

3.2 NOMNT simulation

Diurnal variation of precipitation in case NOMNT is shown in Fig. 8 as an average of the second and the third days. Clearly, instead of the night maximum of precipitation found in case CNTL (Fig. 4), afternoon maximum appeared over the land (290 km $<$ $x <$ 1300 km). Significant long-lived and traveling precipitation systems did not occur over the land although rather weak systems existed. The afternoon maximum of precipitation corresponds to the afternoon minimum of atmospheric stability due to the increasing ground surface temperature in the afternoon. This precipitation occurred mainly during the second day. On the third day, only scattered small cumuli existed with little precipitation.

These differences from CNTL indicate that the mountains located in upstream of the plain govern the night maximum of precipitation by triggering squall lines at approximately the same local time immediately downstream of the mountains. An early morning maximum arose over the ocean near the eastern boundary of the model domain (1400 km $< x$). Considering that this area is near

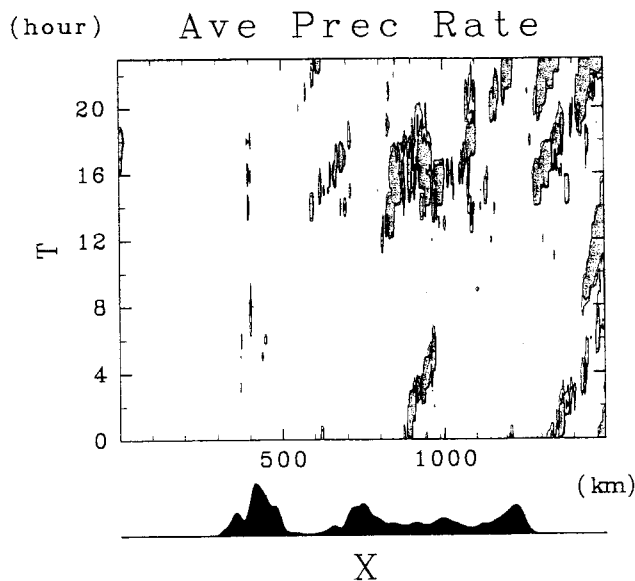the outflow boundary, this precipitation maximum is probably spurious.

Total precipitation amount averaged over land on the second and the third days was 11.4 mm, about 1.5 times smaller than that in CNTL (16.8 mm). Averaging over the inland region only (400 km $<$ $x <$ 1200 km), this ratio was almost the same: 11.2 mm in NOMNT and 17.0 mm in CNTL. Hence, not only did the mountainous terrain determine the phase of diurnal variation of precipitation, but it also enhanced total precipitation amount even over the lee-side areas. This effect of mountains on the total precipitation amount is interesting because it is counter-intuitive; mountains often reduce precipitation over the lee side regions, for example, in foehn or Chinook situations.

3.3 NOSEA simulation

Diurnal variation of precipitation in NOSEA is shown in Fig. 9 as an average of the second and the third day. Precipitation on the upstream side of the Dawna Range (300 km $< x <$ 400 km) simulated in case CNTL (Fig. 4) did not occure. As in CNTL, propagating squall lines over the downstream side of the Dawna Ridge (450 km $< x <$ 700 km) practically disappeared in NOSEA. Both precipitation systems were probably not supplied with sufficient vapor to maintain themselves, because the water vapor fed from the land surface is less than that from the sea surface. On the other hand, precipitation systems over the Khorat Plateau (800 km $< x <$ 1100 km) still remained, though the precipitation pattern was largely modified. In other words, in NOSEA, precipitation systems disappeared over the western half of the Indo-China Peninsula but stayed in the eastern half of the Peninsula. This result indicates that the former systems were supplied with
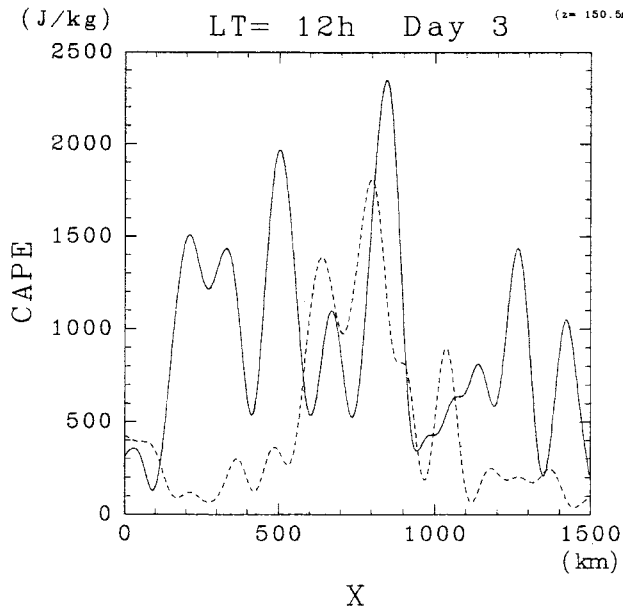
Fig. 10. Horizontal variation of CAPE at the noon of the third day for case CNTL (solid) and case NOSEA (dashed). CAPE is passed low-pass filter with cut-off length of 100 km.
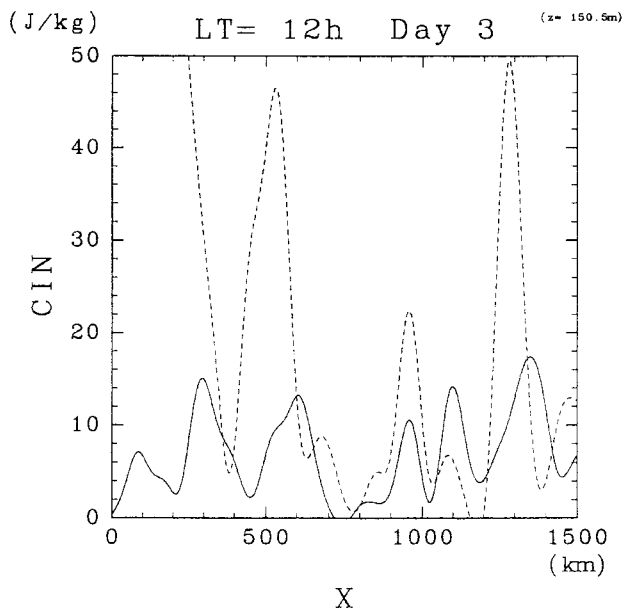

Fig. 11. Same as Fig. 10 except for CIN.
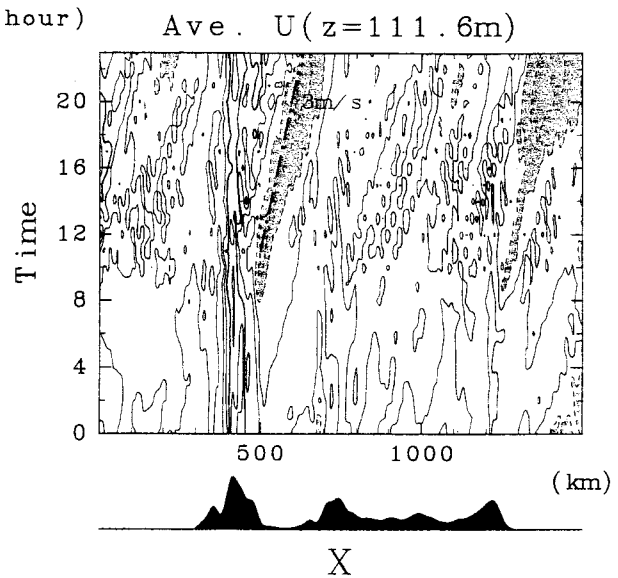

Fig. 12. Horizontal-time section diagram of filtered horizontal velocity u at $\sim$ 100 m above the ground averaged on the second and the third days in case DRY. Contours are ± 1, ± 3, ± 5 and ± 9 m s^{-1}. Shaded area indicates $u < -1$ m s^{-1}. Dash-dotted line indicates moving speed of 3 m s^{-1}. The surface topography is depicted by the black shading at the bottom of the figure.

water vapor from the Andaman Sea, while the latter systems used water vapor fed from the land surface.

Differences of horizontal variations of CAPE (convective available potential energy) and CIN (convective inhibition) between NOSEA and CNTL were consistent with the difference of precipitation systems between them. In case CNTL, CAPE was larger than 1000 J kg^{-1} over the land except in areas of high elevation (Fig. 10), and CIN was less than 20 J kg^{-1} over the whole land (Fig. 11) at noon of the third day. In case NOSEA, CAPE was as small

as 100–400 J kg^{-1} for $x < 600$ km and CIN was larger than several tens to a hundred J kg^{-1}. Over the middle of the land (600 km $< x < 1000$ km), CAPE and CIN in case NOSEA were almost the same as those in case CNTL, which corresponded with active convection over that area.

3.4 DRY simulation

Figure 12 depicts horizontal velocity at the fifth vertical level of the model (about 100 m above the ground) as an average of the second and the third day in case DRY. To examine mesoscale structures in the horizontal velocity, a low-pass filter with cut-off wavelength 20 km was applied along each model level. There are two distinct features: systems moving eastward slowly during the afternoon and the night, and stationary strong westerly flow over the lee slope of the mountains.

The stationary strong westerly wind was noticed over the peaks and leeward slopes of the Dawna Range (400 km $< x < 500$ km). Over the Dong Phraya mountains (700 km $< x < 800$ km) and the Annam Range ($x \approx 1200$ km), the stationary strong-wind regions also occurred but were not significant. The stationary strong wind occurred over the mountain because the horizontal wind increases with height up to ~ 1.5 km at the initial time (Fig. 2) and also because the mountain enhances the horizontal wind on the leeward slope (see, e.g.,
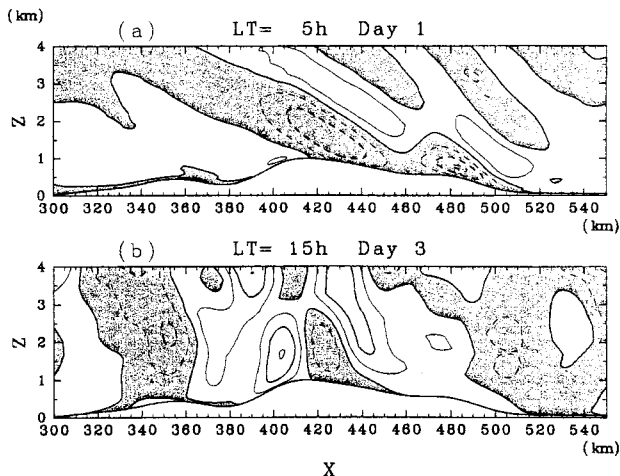
(km)

Fig. 13. Filtered vertical velocity around the Dawna Range at (a) 5 h on the first day and (b) 15 h on the third day in case CNTL. Negative values are shaded. Counter intervals are (a) 0.05 m s^{-1} and (b) 0.1 m s^{-1}.

Smith 1977). The strong wind region was most significant at night but was still noticeable during daytime.

Negative (westward) horizontal wind areas emerged in the morning on the leeward foot of the Dawna Range and the Annam Range. A weak wind area also occurred on the leeward foot of the Dong Phraya mountains in the morning. These negative or weak wind areas started to move in the late morning and were traced till midnight. The travel speed of the $u = 0$ m s^{-1} line was about 3 m s^{-1} eastward, much smaller than the propagation speed of the squall lines in case CNTL (7–10 m s^{-1}).

4. Discussion

4.1 Location and timing of squall line generation

Examining Fig. 7a, it is noticed that upward motion occurred at $x \approx 470$ km before the cold air from the west reached this position. When the leading edge of the cold air arrived, a convective cloud emerged (Figs. 7c and 7d). To examine what determines the initiation location of convective clouds, a low pass filter with 30 km cut-off wavelength along the terrain-following model coordinate ($z^* =$ const.) was applied to the vertical velocity (Fig. 13). At 5 h on the first day when the flow was approximately adiabatic (i.e., no solar heating and no detectable cloud), mountain waves clearly formed over the mountain (Fig. 13a), distinguished by a phase of positive vertical velocity approached the ground around $x = 460$ km near the convection initiation point $x \approx 470$ km. A small bump around $x \approx 480$ km caused the downward extension of the positive vertical velocity. Hence, if a mass of cold air came down the lee slope (katabatic flow), the

upward velocity forced by the leading edge of the cold pool was reinforced by the upward phase of the mountain wave around $x = 460$ km.

Even during the third day afternoon when the thermal and wind structures of the atmosphere were modified by diabatic heating, an area of upward velocity over the lee slope was still evident from 420 km $< x <$ 440 km at $z = 3$ km to 460 km $< x <$ 480 km near the surface. Therefore, we consider that the upward velocity at the front edge of the cold air that penetrated down the lee side of the mountain was reinforced by this area of upward velocity and triggered the squall line each day. This upward velocity was possibly the upward phase of the mountain wave, though greatly modified.

Another interpretation of the reinforcement of the upward motion is as follows: When the cold air ran down the lee slope, the upward velocity forced at its leading edge was not significant due to the descent of the system. When the front edge of the katabatic flow reached flatter terrain (e.g., the foot of the mountain or the small bump at $x \approx 480$ km), the forced ascent triggered the squall line.

The moving squall lines in case CNTL is similar to, but not the same as, the moving zone of ascent over the lee side of the mountain discussed by Fujibe et al. (1999). Using a dry numerical model including the solar radiation, they found that downslope wind and valley wind converged over the lee slope near the mountain top at noon. The zone of upward velocity associated with this convergence slowly moved down on the lee slope during the afternoon. The moving zone of the weak horizontal velocity in case DRY seems to correspond to the moving convergence zone of Fujibe et al. (1999). On the other hand, in case CNTL herein, the cold air embedded in the downslope wind played a major role in producing ascent. In addition, the propagation speeds of squall lines were two-to-three times faster than the speed of the moving zone of weak horizontal velocity in case DRY.

4.2 Observational evidence

An activity index of deep convective clouds I_C is defined by

$$I_c = 230 - T_{BB} \quad : \quad T_{BB} < 230 \text{ K}$$
$$= 0 \qquad \quad : \quad T_{BB} \geq 230 \text{ K}, \quad (3)$$

where T_{BB} is the infrared equivalent black body temperature derived from GMS. Hourly T_{BB} data for one month (June 1996) at $0.05° \times 0.05°$ grid points are utilized for the analysis. Although I_C does not correspond well with rainfall amount for scales much smaller than several hundreds of kilometers (Richard and Harken 1981), it nevertheless indicates the activity of deep clouds such as squall lines.
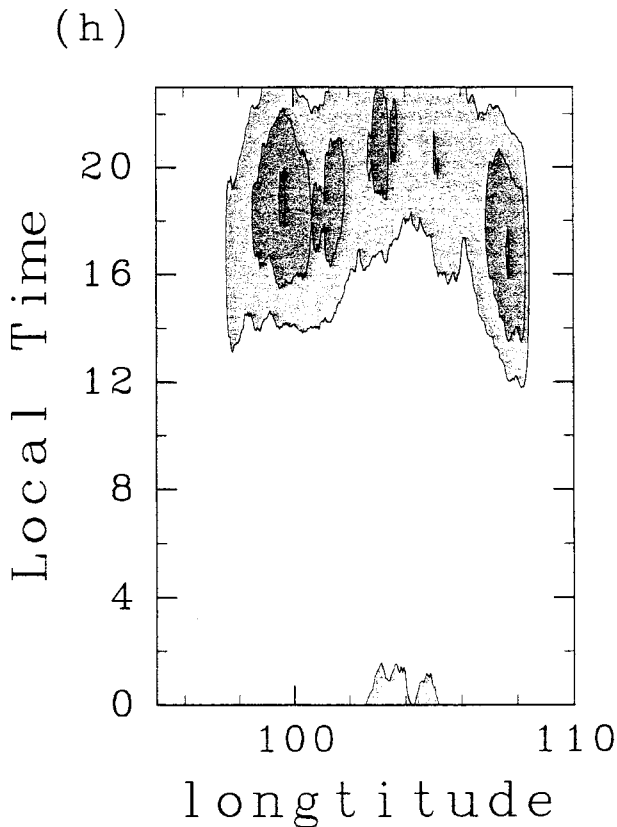
(h)

Fig. 14. Horizontal-time section diagram of amplitudes of diurnal components of I_C at 15°N on June 1996 over the Indo-China Peninsula. Only the positive values are contoured with an interval of 1 K.

Figure 14 shows a horizontal-time section of amplitudes of diurnal components of I_C along a latitude of 15°N over the Indo-China Peninsula. At 15°N, the Dawna Range is located around 99°E and the Dong Phraya mountains around 101.5°E. It is clearly shown that I_C has a trend towards later maximum as increasing longitudes until 104–105°E. This supports the simulation result that the traveling squall line causes the diurnal variability of precipitation. It is also noticeable that the amplitudes of diurnal variability have local minima on the lee side of the Dawna Range and the Dong Phraya mountains, which harmonizes with the precipitation gap in the simulation ($x \approx 400$–450 km and $x \approx 750$ km, see Fig. 4).

A trend towards later maximum at decreasing longitudes over the eastern Indo-China Peninsula (105°–108°E) is observed in Fig. 14. The cause of this westward propagation of cloud activity is not clear, although I_C roughly estimated from simulated clouds also shows the similar westward propagation (not shown).

4.3 Orogenic squall lines in midlatitudes

Triggering and propagation of squall lines on the lee slope of a mountain in the late afternoon are not unique to the Indo-China Peninsula. The same mechanism can work in some orogenic squall lines in midlatitudes. Tripoli and Cotton (1989) reported that the lee-side subsidence suppressed convection in their 2D numerical model over the Rocky Mountains of the U. S.. Further, they suggested a mechanism similar to this study in that deep convection was triggered when an air mass from the windward side of the mountains reached the ascending branch of mountain waves over the lee-side slope. Tucker and Crook (1999) also pointed out the importance of cold air running down the lee slope for the generation of mesoscale convective system; the cold air in their study originated as outflow from previous convective activity over the lee slope of the Rocky Mountains.

Statistical analyses of diurnal variability of precipitation over the Great Plains in summer (Wallace 1975; Riley et al. 1987) show clear trends towards a later maximum eastward from the mountains. These facts indicate that the triggering and propagation of squall lines on the lee-side of mountains are sufficiently common that statistical analyses of long-term precipitation data can detect the eastward phase lag of the diurnal precipitation maximum. Though Tripoli and Cotton (1989) and Tucker and Crook (1999) are specific case studies, in contrast to this paper where climate data were used as the initial conditions, both the numerical simulations and statistical analyses of rain gauge networks suggest that the same mechanisms operate in the diurnal variability of summer precipitation eastward of mountain ranges in midlatitudes as well as in the tropics.

5. Summary

Diurnal variation of precipitation over the Indo-China Peninsula was simulated by a two-dimensional, nonhydrostatic, and cloud-resolving numerical model. Conclusions are as follows:

1) Convection triggered at the lee-side foot of mountains in the late afternoon forms squall lines which propagate eastward and produce night maxima of precipitation in inland areas far eastward from the mountain.

2) The timing and location of convection initiation are determined by the intrusion of cold air from the windward side into the lee side and also by the mountain wave.

3) The Andaman Sea feeds water vapor that causes precipitation over the lee side of the Dawna Range. Water vapor that maintains pre-

cipitation over the eastern half of the Peninsula comes mainly from the land surface.

4) Orogenic squall lines (CNTL) brought 1.5 times more precipitation than cloud systems over flat land (NOMNT).

5) The simulated night maxima of diurnal variation of precipitation and eastward propagation of convectively active systems was confirmed by the high resolution analysis of I_C .

The mechanism behind the daily triggering of convection probably works in other summer precipitation systems in the lee side of mountains. In this study, climatic thermal and wind conditions were used as the initial data for the model. The proposed mechanism required only a general element in addition to the environment preferable for squall lines: the cold air mass advected from the windward side of the mountain reaches a flat terrain in the lee side where the up-branch of mountain wave approaches the surface. Considering that neither the initial condition of the model nor the simulated precipitation diurnal cycle in this study are associated to one special event in the Indo-China Peninsula, the daily variation of precipitation over several tropical regions are most probably explained by the mechanism proposed herein. For example, a similar phase shift of diurnal I_C variation is detectable over Borneo as well as over the Indo-China Peninsula in the analysis of Nitta and Sekine (1994) using low resolution ($1° \times 1°$) data of T_{BB} (Fig. 4a of their paper). Considering that there is a high mountain range (Iran Mountains) elongated from southwest to northeast in Borneo, the phase shift over Borneo is arguably caused by the triggering and propagation of squall lines over the lee side of the Iran Mountains.

In contrast to the analysis of I_C, whose maximum time was about 2 hours later than the maximum time of precipitation over the Malay Peninsula (Oki and Mushiake 1994), the analysis of radar data directly reveals not only the maximum time but also the structures of the precipitation systems. Single radar has a limited observation range about 100–200 km. Fortunately, in Thailand, a Doppler radar network covers the whole nation. Analysis of those radar data during monsoon seasons now proceeds in cooperation with the Thai Meteorological Department.

Acknowledgments

References

Albright, M.D., E.E. Recker, R.J. Reed and R. Dang, 1985: The diurnal variation of deep convection and infrared precipitation in the central tropical Pacific during January–February 1979. *Mon. Wea. Rev.*, **113**, 1663–1680.

Arkin, P.A. and B.N. Meisner, 1987: The relationship between large-scale convective rainfall and cold cloud over the Western Hemisphere during 1982–84. *Mon. Wea. Rev.*, **115**, 51–74.

Asai, T., S. Ke and Y. Kodama, 1998: Diurnal variability of cloudiness over East Asia and the western Pacific Ocean as revealed by GMS during the warm season. *J. Meteor. Soc. Japan*, **76**, 675–684.

Avissar, R. and R.A. Pielke, 1989: A parameterization of heterogeneous land surface for atmospheric numerical models and its impact on regional meteorology. *Mon. Wea. Rev.*, **117**, 2113–2136.

Chong, M., P. Amyenc, G. Scialom and J. Testud, 1987: A tropical squall line observed during the COPT 81 Experiment in West Africa. Part I: Kinematic structure inferred from dual Doppler radar data. *Mon. Wea. Rev.*, **115**, 670–694.

Clark, T.L., 1977: A small-scale dynamic model using a terrain-following coordinate transformation. *J. Comput. Phys.*, **24**, 186–215.

Dickinson, R.E., A. Henderson-Sellers, P.J. Kennedy and M.F. Wilson, 1986: Biosphere-Atmosphere Transfer Scheme (BATS) for the NCAR Community Climate Model. TN-275+STR, NCAR.

Duvel, J.P. and R.S. Kandel, 1985: Regional-scale diurnal variations of outgoing infrared radiation observed by METEOSAT. *J. Climate Appl. Meteor.*, **24**, 335–346.

Fujibe, F., K. Saito, D.S. Wratt and S.G. Bradley, 1999: A numerical study on the diurnal variation of low-level wind in the lee of a two-dimensional mountain. *J. Meteor. Soc. Japan*, **77**, 827–843.

Gal-Chen, T. and R.C.J. Somerville, 1975: On the use of a coordinate transformation for the solution of the Navier-Stokes equations. *J. Comput. Phys.*, **17**, 209–228.

Harada, S., T. Oki and K. Mushiake, 1998: Diurnal variation and its seasonal variation of convective activity over the Indochina Peninsula region by GMS-IR data, *J. Japan Soc. Hydrol. Water Resour.*, **11**, 371–381 (in Japanese).

Hauser, D., F. Roux and P. Amayenc, 1988: Comparison of two methods for the retrieval of thermodynamic and microphysical variables from Doppler radar measurements: Application to the case of a tropical squall line. J. Atmos. Sci., 45, 1285–1303.

Janowiak, J.E., P.A. Arkin and M. Morrissey, 1994: An examination of the diurnal cycle in oceanic tropical rainfall using satellite and in situ data. Mon. Wea. Rev., 122, 2296–2311.

Karr, T.W. and R.L. Wooten, 1976: Summer radar echo distribution around Limon, Colorado. Mon. Wea. Rev., 104, 728–734.

Klemp, J.B. and R.B. Wilhelmson, 1978: The simulation of three-dimensional convective storm dynamics. J. Atmos. Sci., 35, 1070–1096.

Landin, M.G. and L.F. Bosart, 1985: Diurnal variability of precipitation in the northeastern United States. Mon. Wea. Rev., 113, 989–1014.

Lin, Y.-L., R.L. Deal and M.S. Kulie, 1998: Mechanisms of cell regeneration, development, and propagation within a two-dimensional multicell storm. J. Atmos. Sci., 55, 1867–1886.

Liu, C. and M.W. Moncrieff, 1998: A numerical study of the diurnal cycle of tropical oceanic convection. J. Atmos. Sci., 55, 2329–2344.

Meisner, B.N. and P.A. Arkin, 1987: Spatial and annual variations in the diurnal cycle of large-scale tropical convective cloudiness and precipitation. Mon. Wea. Rev., 115, 2009–2032.

Moncrieff, M.W. and M.J. Miller, 1976: The dynamics and simulation of tropical cumulonimbus and squall lines. Quart. J. Roy. Meteor. Soc., 102, 373–394.

Murakami, M., 1983: Analysis of the deep convective activity over the western Pacific and Southeast Asia. Part I: Diurnal variation. J. Meteor. Soc. Japan, 61, 60–76.

Nakajima, T., M. Tsukamoto, Y. Tsushima and A. Numaguti, 1995: Modelling of the radiative process in a AGCM. Climate System Dynamics and Modelling, Reports of A New Program for Creative Basic Research Studies, I-3, T. Matsuno, Ed., Center for Climate System Research, 104–123.

Nitta, T. and S. Sekine, 1994: Diurnal variation of convective activity over the tropical western Pacific. J. Meteor. Soc. Japan, 72, 627–641.

Oki, T. and K. Mushiake, 1994: Seasonal change of the diurnal cycle of precipitation over Japan and Malaysia. J. Appl. Meteor., 33, 1445–1463.

Pielke, R.A., W.R. Cotton, R.L. Walko, C.J. Tremback, W.A. Lyons, L.D. Grasso, M.E. Nicholls, M.D. Moran, D.A. Wesley, T.J. Lee and J.H. Copeland,

1992: A comprehensive meteorological modeling system - RAMS. Meteorol. Atmos. Phys., 49, 69–91.

Randall, D.A., Harshvardhan and D.A. Dazlich, 1991: Diurnal variability of the hydrologic cycle in a general circulation model. J. Atmos. Sci., 48, 40–62.

Reed, R.J. and K.D. Jaffe, 1981: Diurnal variation of summer convection over West Africa and the tropical eastern Atlantic during 1974 and 1978. Mon. Wea. Rev., 109, 2527–2534.

Richard, F. and P. Arkin, 1981: On the relationship between satellite-observed cloud cover and precipitation. Mon. Wea. Rev., 109, 1081–1093.

Riley, G.T., M.G. Landin and L.F. Bosart, 1987: The diurnal variability of precipitation across the central Rockies and adjacent Great Plains. Mon. Wea. Rev., 115, 1161–1172.

Saito, T. and F. Kimura, 1998: Diurnal variation of convective precipitation in Chubu-Kanto area in the summer, Tenki, 45, 541–549 (in Japanese).

Schwartz, B.E. and L.F. Bosart, 1979: The diurnal variability of Florida rainfall. Mon. Wea. Rev., 107, 1535–1545.

Seitter, K.L., 1986: A numerical study of atmospheric density current motion including the effects of condensation. J. Atmos. Sci., 43, 3068–3076.

Smith, R.B., 1977: The influence of mountains on the atmosphere. Adv. Geophys., 21, 87–230.

Sui, C.-H., X. Li and K.-M. Lau, 1998: Radiative-convective processes in simulated diurnal variations of tropical oceanic convection. J. Atmos. Sci., 55, 2345–2357.

———, K.-M. Lau, Y.N. Takayabu and D.A. Short, 1997: Diurnal variations in tropical oceanic cumulus convection during TOGA COARE. J. Atmos. Sci., 54, 639–655.

Tao, W.-K. and J. Simpson, 1989: Modeling study of a tropical squall-type convective line. J. Atmos. Sci., 46, 177–202.

Tripoli, G.J. and W.R. Cotton, 1989: Numerical study of an observed orogenic mesoscale convective system. Part 1: Simulated genesis and comparison with observations. Mon. Wea. Rev., 117, 273–304.

Tucker, D.F. and N.A. Crook, 1999: The generation of a mesoscale convective system from mountain convection. Mon. Wea. Rev., 127, 1259–1273.

Wallace, J.M., 1975: Diurnal variations in precipitation and thunderstorm frequency over the continental United States. Mon. Wea. Rev., 103, 406–419.

Zipser, E.J., 1977: Mesoscale and convective-scale downdrafts as distinct components of squall-line structure. Mon. Wea. Rev., 105, 1568–1589.

インドシナ半島の降水日変化
－2次元数値実験－

里村雄彦

（京都大学大学院理学研究科）

　2次元非静水圧雲解像モデルを用い、インドシナ半島の降水日変化について調べた。モデルの初期値は、インドシナ半島のほぼ中央である東経 102.5 度北緯 17.5 度における 6 月気候値の風速・気温・湿度の鉛直分布から作成した。

　モデルは観測されている日変化の特徴をうまく再現することができた。モデルによる日変化は、1) タイ西部と中央部に位置する山地の風下側山麓において対流雲が夕方に励起され、2) それらがスコールラインに組織化されて夜間に東へ移動して行く、という現象の繰り返しで起こっている。このスコールラインの移動速度は 5–10 m s^{-1} であった。また、風下山麓での対流励起機構やスコールラインの構造について検討し、中緯度での観測や数値実験との比較も行った。

　これらの計算結果に基づき、太陽同期したスコールラインの発生と東への移動がインドシナ半島内陸部の降水日変化の夜の極大をもたらしている、と結論した。高分解能の対流活動指数を用いた対流雲活動の日変化の空間分布も解析し、数値実験を支持する結果を得た。